Materials Advances

ROYAL SOCIETY OF CHEMISTRY

COMMUNICATION

View Article Online
View Journal | View Issue

Cite this: *Mater. Adv.*, 2024, 5, 504

Received 11th October 2023,
Accepted 27th November 2023

DOI: 10.1039/d3ma00837a

rsc.li/materials-advances

Mica nanosheets synthesized *via* liquid Ga embrittlement: demonstrating enhanced CO_2 capture†

P. Vishakha T. Weerasinghe,[a] Shunnian Wu,[a] W.P. Cathie Lee,[a] Qiang Zhu,[b] Ming Lin[b] and Ping Wu*[a]

We introduce a pioneering approach to synthesize 2D mica nanosheets by leveraging the liquid gallium embrittlement mechanism, effectively addressing the challenges involved in exfoliating mica due to its strong non-van-der-Waals bonds. To gain insights into the underlying mechanisms, including energy barrier determination in liquid metal embrittlement and biaxial straining, and to provide valuable guidance for designing 2D nanosheet synthesis, we propose an integrated model that incorporates first-principles calculations, biaxial straining principles, and experimental design. Our experimental findings demonstrate the successful exfoliation of mica nanosheets with lateral dimensions ranging from 100 to 300 nm and thicknesses ranging from 1 to 15 nm. Remarkably, we found a significant reduction in resistance, from 50 ± 8 MΩ for natural mica to 28 ± 10 MΩ for Ga-intercalated mica. Moreover, when compared to natural mica, these 2D mica nanosheets exhibit a remarkable 76% enhancement in CO_2 capture efficiency. This work advances the synthesis of 2D materials and contributes to a comprehensive understanding and effective management of liquid metal embrittlement phenomena, paving the way for a groundbreaking approach to 2D structure synthesis.

Introduction

Two-dimensional (2D) materials have gained increasing attention since the discovery of graphene in 2004.[1] Most of these 2D materials are often formed by exfoliating the corresponding three-dimensional (3D) bulk, where the crystal planes are held together by weak van der Waals forces. However, the strict requirement of van der Waals nature confines a library of 2D materials, excluding the vast majority of industrially viable and commercially utilized materials. Thus, a new and diverse class of 2D materials is emerging from non-van der Waals (non-vdW) 2D solids.[2]

2D mica sheets are a fascinating material obtained through the exfoliation of their bulk counterpart, which naturally exists as a 3D non-van der Waals layered material. These 2D mica sheets outperform graphene as an anticorrosive agent.[3] Mica is also used in many other fields, such as cell growth,[4] electron tunneling devices,[5] flexible and transparent devices[6] and CO_2 capture[7] and separation.[8] The present study focuses on muscovite mica ($KAl_3Si_3O_{10}\cdot(OH)_2$), whose chemical structure is represented by an octahedral layer of alumina sandwiched between two identical tetrahedral layers of silica, separated by a layer of potassium ions. This results in strong Coulombic interactions between neighboring layers, making the exfoliation process challenging. Some reported techniques for mica exfoliation include liquid phase exfoliation using ions' or molecules' intercalation followed by sonication,[3,5,6,8–10] as well as mechanical exfoliation using scotch tape. However, these current exfoliation approaches often require difficult experimental setups, hazardous chemical reagents, excessive energy consumption, or lengthy processing times. Therefore, there is a need for a scalable method to produce mica nanosheets of high quality.

Liquid-metal embrittlement (LME) happens when intrinsically ductile metals, such as Al, Ni, and Cu, contact with liquid metals (LM) such as Ga and Bi, which brings about intergranular failure with exceptionally dramatic stress loss. The mechanism consists of two basic steps: (1) crack initiation at the site of contact between the aggressive liquid metal and the solid sample, and (2) rapid crack propagation along grain boundaries.[11] LME has raised concern due to liquid metal-induced damage in aircraft,[12] nuclear reactors, and the corrosion and embrittlement caused by a liquid alloy.[13] There have been incidents like the Flixborough damage caused by molten zinc on stainless steel.[14] In this work, we take advantage of the

[a] *Entropic Interface Group, Engineering Product Development, Singapore University Technology and Design, Singapore. E-mail: wuping@sutd.edu.sg*
[b] *Institute of Materials Research and Engineering (IMRE), A*STAR (Agency for Science, Technology and Research), 2 Fusionopolis Way, Singapore 138634, Singapore*

† Electronic supplementary information (ESI) available. See DOI: https://doi.org/10.1039/d3ma00837a

properties of LME to exfoliate layer-structured materials in spite of these negative consequences.

Although there are several models that attempt to explain LME, a comprehensive understanding of its fundamental mechanisms is still unattainable. Among the models that are currently used are the Reduction in Surface Energy (RSE) model, the Adsorption Induced Reduction in Cohesion Model (AIRCM), the Enhanced Dislocation Emission (EDE) Model, and the Dissolution-Condensation Mechanism (DCM).[15] These models were developed through computational or experimental means. First-principles calculations have been used to describe LME phenomena at the atomic scale for solid materials such as steel, Mg, Al, Ti and their alloys with liquid metals such as Hg, Ga, Bi, Pb, Sn, Zn and Cd through interatomic bonding energy, solubility, vacancy formation, and intermetallic formation.[16] However, the challenge is determining the occurrence of embrittlement for a particular solid–liquid metal element system under specific test conditions, which is known as the specificity of LME.[17]

Here, we examined the main factor influencing the specificity of LME for a Ga–mica system using first-principles calculations for the first time. By incorporating these calculated results and biaxial straining principles, we propose a novel model for fast crack propagation in layered materials *via* LME. We evaluated the exfoliation ability based on LME through experiments. The exfoliated mica *via* Ga intercalation is comprehensively characterized in terms of morphology, elemental composition, and electrical resistivity, suggesting a viable approach for the scalable exfoliation of 2D nanosheets. Additionally, we assess the CO_2 capture performance, demonstrating the applicability of Ga-intercalated mica nanosheets for CO_2 capture.

Materials and methods

Computational simulations

The first-principles calculations were carried out using a periodic supercell model employing the Vienna *Ab initio* simulation package (VASP)[18,19] with the Perdew–Burke–Ernzerhof (PBE) generalized gradient approximation (GGA) exchange–correlation functional.[20] A projector augmented wave (PAW) method[19,21] was adopted with a 500 eV energy cutoff. The van der Waals (vdW) corrected functional (DFT+D3 correction method[22]) was incorporated in all mica calculations. A Monkhorst–Pack *K*-points mesh[23] was adopted for sampling the Brillouin zone, where the number of *K*-points, NK, is adjusted to maintain NK × *L* (*L* is the lattice constant) about 45 Å for structural optimization and 75 Å for electronic calculations, respectively. The internal optimization is converged with the force on each atom to be less than 0.01 eV $Å^{-1}$. The energy convergence with respect to the *k*-points and cutoff energy has been tested to be less than 0.01 eV per cell.

The stable structure of mica has been obtained in our previous work.[10] The smallest repeated unit adopted for calculations is the 1 × 1 × 2 supercell containing 84 atoms. One, two and four Ga atoms are gradually introduced into the interlayer of mica in this work, which are denoted as 1ga-mica, 2ga-mica and 4ga-mica, respectively. Their ground configurations were obtained by performing full geometry optimization. Their formation enthalpy E_f is calculated using the equation $E_f = 12E_{Al} + 12E_{Si} + 48E_O + 8E_H + n_{Ga}E_{Ga}$, where n_{Ga} is the amount of inserted Ga atoms, E_O and E_H refer to the energy per atom in O_2 and H_2 gas, which are the most stable elementary form of O and H under ambient conditions, respectively. E_{Al}, E_{Si} and E_{Ga} are energy per atom for metals Al, Si, and Ga, each in the form of its own most stable elementary substance, respectively.

The interlayer spacing is defined as $D_{int} = Z_{oh} - Z_{ol}$, where Z_{oh} and Z_{ol} are the averaged Cartesian *z* coordinates of three lowest oxygen atoms among the oxygens forming tetrahedrons in the upper sheet and of three highest oxygen atoms among the oxygens forming tetrahedrons in the lower sheet, respectively. To calculate the exfoliation energy E_{exf} for the mica, their two sheets and one sheet placed in a supercell were constructed and fully optimized to determine their total energy E_{2L} and E_{1L}, respectively.[24] The cleavage plane was placed normal to the *c* axis, and the lattice parameters *a* and *b* and *β* were set as the calculated lattice constants of the corresponding bulk mica. At least 20 Å vacuum to eliminate the impact of periodic boundary conditions is imposed on these mica nanosheets. Half of the interlayer cations were separated on each side of the mica nanosheets surface, with the initial cation position at the center of the corresponding hexagonal tetrahedral ring. E_{exf} is calculated as $E_{exf} = E_{2L} - 2E_{1L}$. To further calculate the exfoliation energy E_{exf} for the Ga-inserted micas, Ga atoms are placed and removed on up and down one sheet, respectively, which are denoted as E_{1UG}, E_{1U}, E_{1DG} and E_{1D}, and E_{exf} is calculated as

$$E_{exf} = E_{2L} - \frac{(E_{1U} + E_{1D} + E_{1UG} + E_{1DG})}{2}.$$

Materials and reagents

Natural ground muscovite mica of 99.5% purity was obtained from Huajing mica Co. Ltd (Shijiazhuang City, China). Gallium ingot (99.9999%) was purchased from VWR Singapore Pte Ltd.

Ga intercalation assisted mica exfoliation

For exfoliation of ground mica, 4 g of natural mica was first mixed with 0.4 g of Ga using a motor and pestle for 30 minutes. To keep Ga in the liquid state, the temperature of the motor was maintained at about 45 °C using a hot plate. The mixed sample was kept in the oven at 60 °C for 30 minutes. Then, the sample was divided into two equal weights and put into two 100 ml grinding vessels. Grinding was performed in a dry environment using 90 g grinding balls of sizes 3, 5, 10 and 15 mm in Ziconia vessels (Changsha Tianchuang Powder Technology CO., Ltd). The spinning speed of the high energy planetary ball mill was maintained at 600 rpm for 30 minutes. The obtained powder was sonicated (5 s pulse and 2 s rest) for 1 hour using a Q125 Tip Sonicator with a variable power of 0–500 W and a vibration frequency of 20 kHz (Qsonica L.L.C.). The final product was centrifuged at 6000 rpm for 10 min to remove the unexfoliated mica.

Instrumental characterization

Mica sheet morphology was evaluated using scanning electron microscopy (SEM) JEOL JSM-7600F coupled with energy dispersive X-ray spectroscopy (EDS) and FEI Titan 80/300 Scanning/Transmission Electron Microscopy (TEM) (200 KV). For electrical resistivity measurements, 4.5 g powder samples were pressed into pellets measuring 13 mm in diameter and 1.4 mm in thickness using a Manual Hydraulic Press (FTIR + XRF Pellet Press, Specac, UK). The resistance between two sides of the cylindrical pallet was measured using two probes (Fluke 289 True- RMS Data Logging Multimeter). The resistance between two faces of the cylindrical pallet was measured using a two probes method (Fluke 289 True-RMS Data Logging Multimeter). CO_2 capturing performance was tested using a Thermo Gravimetric Analyzer (TGA, TGA Q50 analyzer, TA Instruments, New Castle, DE, USA). To perform CO_2 adsorption TGA analysis, ~6.5 mg samples were loaded onto a platinum (Pt) pan within the TGA apparatus. To prevent errors arising from pre-adsorbed species, including ambient CO_2, water, and other contaminants, the samples underwent pre-treatment at 150 °C for 60 minutes. This pre-treatment was carried out under a high-purity N_2 flow rate of 40 mL min^{-1}, with the temperature being raised at a rate of 10 °C min^{-1}. Subsequently, the gas was changed from N_2 to pure CO_2 (1 atm, 40 ml min^{-1}), while the temperature was gradually lowered to 30 °C at a rate of 10 °C min^{-1}. The sample was then maintained in this 100% CO_2 atmosphere for a period of 90 minutes, during which the weight change of the sample was continuously monitored in relation to both temperature and time. The CO_2 adsorption capacity can be precisely determined by the measurement of the weight change.

Results and discussion

Energy barrier determination *via* first-principles calculations

In this phase of the study, we aimed to gain insights into the mechanism underlying Ga-intercalated mica's LME (Layered Mica Expansion). To achieve this, we evaluated the energy barrier related to fracture propagation using first-principle calculations. In particular, our first-principle calculations included two crucial elements:

(1) Examining the feasibility of intercalating gallium atoms—namely, one, two, and four gallium atoms, denoted as 1Ga mica, 2Ga mica, and 4Ga mica, respectively (as depicted in Fig. 1).

(2) Determining the energy barrier in the presence of gallium, concentrating on the formation energy of the Ga/mica surface.

First, as shown in Fig. 1, we investigated the viability of intercalating gallium atoms into mica, including one, two, and four gallium atoms, which are referred to 1Ga-mica, 2Ga-mica, and 4Ga-mica, respectively. It was found that the energy required for Ga incorporation decreases significantly with increasing number of Ga atoms inserted into the mica interlayers, which is due to the formation of Ga2 and Ga4 clusters: $E_{cluster}$ Ga2 − 1.66 eV and $E_{cluster}$ Ga4 − 0.99 eV (Table 1), where

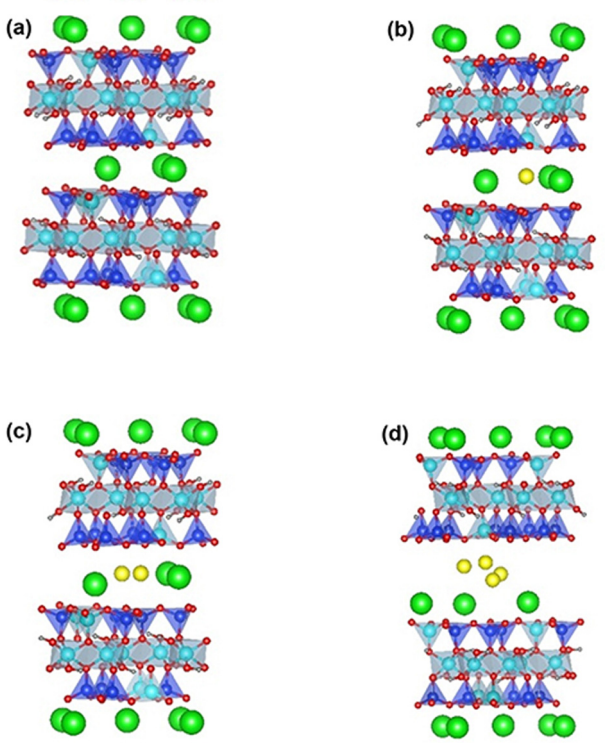

Fig. 1 Optimized structure of parent mica (a) and 1Ga-mica (b), 2Ga-mica (c), and 4Ga-mica (d). The red, blue, cyan, green, yellow, and grey balls represent O, Si, Al, K, Ga, and H atoms, respectively.

Table 1 Energy required for inserting a Ga atom into mica and the formation enthalpy E_f of the yielded mica

	$E_{cluster}$ (eV)	E_f (eV)	Bandgap (eV)
Mica		−230.71	4.92
1Ga-mica	3.40	−227.31	4.35
2Ga-mica	1.66	−227.38	1.25
4Ga-mica	0.99	−226.77	0.63

$E_{cluster} = (E_{nGa\text{-}mica} - E_{mica} - nE_{Ga})/n$ with $E_{nGa\text{-}mica}$, E_{mica} and E_{Ga}, represents the total energy of mica with inserted Ga, parent mica and Ga, respectively, and n represents the number of inserted Ga. Additionally, the electronic band gap was lowered from 4.92 eV for mica to 0.63 eV for 4Ga-mica by inserting Ga atoms (Table 1).

We then turned our attention to the formation energy of the Ga/mica surface and proceeded to evaluate the energy barrier in the presence of gallium. According to the Griffith theory,[25] crack propagation (Fig. 2(a)) occurs when the reduction in potential energy, which is in the form of strain energy U (Fig. 2(b)), equals or surpasses the increase in surface energy W (Fig. 2(b)) as a result of a crack's expansion. This increase in surface energy is associated with the creation of new free surfaces as the crack spreads.

The critical event of crack propagation occurs when the crack length l reaches l_c (Fig. 2(b)), at which point the total energy T (Fig. 2(b)) reaches its maximum value, known as T_{max}

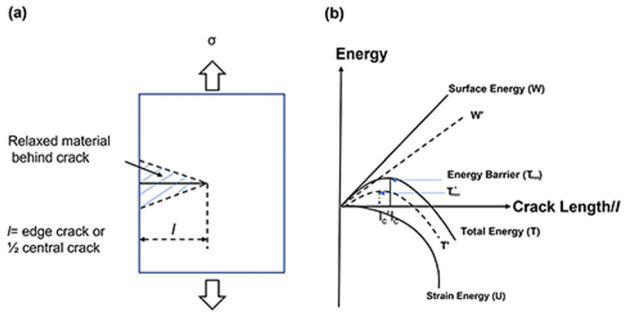

Fig. 2 (a) Sketch of a micro edge crack with length l. (b) Schematic illustration of Griffith's theory of energetics of crack propagation.

Table 2 Calculated interlayer distance and exfoliation energy of parent mica and Ga inserted mica

	D_{int} (Å)	E_{exf} (eV)
Mica	3.49	−3.05
1Ga-mica	4.56	−2.72
2Ga-mica	5.02	−2.29
4Ga-mica	7.11	−1.95

(Fig. 2(b)). The energy barrier stopping fracture growth is this maximum energy. An unstable state arises from the energy balance between U and W: when $U < W$, it corresponds to a sealed crack for which the crack length, $l < l_c$. On the other hand, when $U \geq W$, it indicates crack growth, where the crack length, $l \geq l_c$.

In this work, we described a method that lowers surface formation energy in order to speed up fracture propagation. This is accomplished by shifting the mica layers from W to W' by inserting Ga between them. Therefore, we predict that this strategy will cause the total energy T to change to T' (depicted in Fig. 2(b)), and the energy barrier T_{max} (Fig. 2(b)) may decrease to zero or even become negative (T'_{max} of Fig. 2(b)). As a result, it is expected that the critical crack length (l_c), denoted as l'_c, will drop (Fig. 2(b)). This reduction in critical crack length is anticipated to facilitate rapid crack propagation when Ga is present.

The formation energy of mica/Ga–mica surfaces is approximated using the formation enthalpies E_f provided in Table 2. Consequently, the decrease in the energy barrier can be quantified by the reduction in the formation energies, as indicated by eqn (1):

$$E_{f\text{-reduction}} = E_{f(air/mica)} - E_{f(Ga/mica)} \quad (1)$$

where $E_{f\text{-reduction}}$ denotes the energy barrier's reduction with respect to formation energies. The formation energy of parent mica is denoted as $E_{f(air/mica)}$, being 230.71 eV. Therefore, in comparison to pure mica, the energy barrier experiences a reduction of 1.3% for 1Ga-mica and 1.7% for 4Ga-mica. This equates to a total increase in the energy barrier reduction percentage from 1Ga-mica to 4Ga-mica of 30.7%.

Additionally, the interaction of Ga between the layers was evaluated by looking at exfoliation energies. Compared to pure mica, it was found that exfoliation energy for 2Ga-mica and 4Ga-mica dropped by 25% and 36%, respectively. Interestingly, when compared to pure mica, the calculated interlayer distances also showed significant increases, expanding by 1.43 times and 2.04 times, respectively.

It may be concluded that the insertion of Ga efficiently promotes the rapid fracture process based on the decrease in the energy barrier, the decreased exfoliation energy, and the increased interlayer spacing.

Biaxial straining model

The analysis of biaxial straining offers crucial information on the underlying mechanisms in the investigation of Ga-inserted mica exfoliation. Applying forces along two perpendicular axes is known as biaxial straining, and it leads to complex deformation behaviour in materials. The Poisson ratio can be used to calculate the material's response to biaxial straining. It helps us better understand the mechanical stability and deformation properties of Ga-inserted mica.

Subsequently, the lattice parameters of all studied mica samples were determined through first principles calculations using density functional theory (DFT) and the results from the calculations are summarized in Table 3. Assuming that the loading force is perpendicular to the *ab* plane, Table 3 lists the strains in three directions ε_a, ε_b, and ε_c, and Poisson ratio ν_a and ν_b calculated using the lattice parameters. Table 3 illustrates that the intercalation of 1Ga atom, 2Ga atoms and 4Ga atoms all bring about positive tensile strain ε_c, hence validating our assumption of the loading force direction. This agrees with the determined Poisson ratio ν_a and ν_b, which indicates the degree of deformation of an object in the direction perpendicular to the loading force. It has been observed that the Poisson ratio decreases with an increase in the number of intercalated Ga atoms.

According to a theory established by our group, strain entropy is the driving force behind the exfoliation of non-van-der-Waals crystals, as delineated by eqn (2).[26,27]

$$\Delta S = \frac{1}{T\alpha}\left(\frac{E_0 + (1-\nu)M\varepsilon}{2}\varepsilon^2 - \frac{A}{r_i}\varepsilon\right) \quad (2)$$

Table 3 Poisson ratio for the Ga intercalated mica samples

	A	b	c	$\varepsilon_a = \frac{\Delta a}{a_0}$	$\varepsilon_b = \frac{\Delta b}{b_0}$	$\varepsilon_c = \frac{\Delta c}{c_0}$	$\nu_a = \frac{-\Delta a}{\Delta c}$	$\nu_b = \frac{-\Delta b}{\Delta c}$	$(1-\nu)M$	ΔP	P_2
mica	5.215	9.046	20.358								
1Ga-mica	5.214	9.028	21.261	−0.0003	−0.0020	0.0444	0.0197	0.0016	19.60	2.25	2.63
2Ga-mica	5.189	9.049	21.888	−0.0050	0.0003	0.0752	0.0017	−0.0171	21.25	1.78	2.23
4Ga-mica	5.196	9.040	23.898	−0.0037	−0.0006	0.1739	0.0016	0.0055	24.76	1.02	1.53

where α and A are the wetting constant (= −0.63) and the constant of coulomb potential, r_i is the lattice constant in the strain-free state, T represents temperature, E_0 denotes the surface Young's modulus, ν stands for Poisson's ratio, and ε represents the tensile strain. This formula is based on the Born–Oppenheimer approximation theory. It takes into consideration the interactions between electronic, nuclear, electron–phonon, and phonon–phonon coupling interactions separately. Its purpose is to identify the origins of strain entropy within a solid.[26] The total entropy change (ΔS) includes modifications in the linear (S1), quadratic (S2), and cubic (S3) components of eqn (2). The linear and quadratic components represent the initial stress entropy originating from electron–electron interactions, which are governed by Coulomb's equation, and electron–phonon interactions resulting from lattice distortions, respectively. The cubic component in this equation symbolizes the interaction between phonons, which gives rise to yield strength, breaks bonds, and initiates plastic deformation. Here, the variable M within the equation represents alterations in the entropy related to phonon–phonon coupling under biaxial loading conditions. This factor assumes a primary role, progressively intensifying until it surpasses a tensile threshold, ultimately leading to the exfoliation of layers due to bond rupture. Therefore, eqn (2) can be employed to evaluate the effects of stress or strain during the substitution process on changes in entropy caused by the intercalation of 1Ga, 2Ga and 4Ga in the interlayers.

Wu *et al.*[28] conducted a theoretical study wherein they examined the thermodynamic aspects of entropy modification resulting from mechanical loading. This concept was validated through experiments conducted by Wu and Tan *et al.*,[28,29] which involved surface wetting measurements on NiTi thin films. They introduced eqn (2) to describe the stress–strain nonlinear deformation from entropy changes on the surface. Therefore, eqn (2) can be understood as a cubic polynomial denoted as $\Delta\theta(\varepsilon) = \Delta S + A\varepsilon + B\varepsilon^2 + C\varepsilon^3$, in which θ represents the water contact angle. According to Young's equation, this angle depends on surface tension, which is affected by surface straining.

The $(1-\nu)M$ term constitutes a component of coefficient C. Both M and $(1-\nu)$ increase as the number of inserted Ga atoms rises. Table 3 demonstrates that $(1-\nu)M$ increases by 26% with the insertion of Ga atoms, progressing from 1Ga to 4Ga. A larger value of $(1-\nu)M$ leads to significant alterations in the cubic component of eqn (2), implying that the entropy contribution from phonon–phonon interactions is likely to play a dominant role. Consequently, this improves the contact angle of intercalated Ga between the layers. An increased contact angle augments the driving force for layer separation, which is the vertical component of the surface tension ($\gamma_{LV}\sin\theta$) of Ga, as depicted in Fig. 3. As a result, this promotes the detachment of surface mica layers from the bulk particle. An even higher stress is induced in the vertical direction, as indicated by the significant increase in $\gamma_{LV}\sin\theta$ due to the dominance of the cubic term ε^3 in eqn (2). This escalation ultimately reaches a tensile threshold, causing layer exfoliation through primary bond breakage.

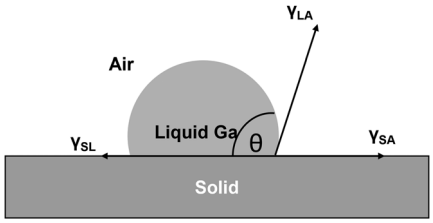

Fig. 3 Sketch of a liquid Ga drop on a solid substrate with the surface free energy and contact angle as described by Young's equation where γ_{LV} = liquid surface free energy, γ_{SV} = solid surface free energy and γ_{SL} = solid/liquid interfacial free energy.

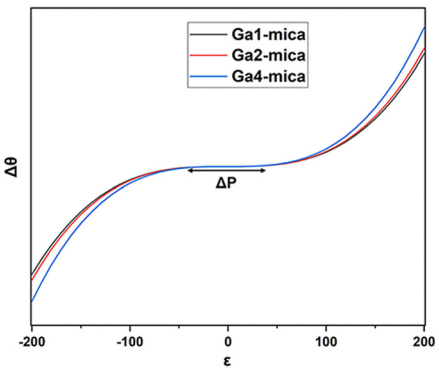

Fig. 4 Contact angle change with tensile strain on the Ga intercalated mica samples.

As a measure of the biaxial straining impact that is represented by the quadratic and cubic terms in eqn (2), the extent of the plateau region (illustrated in Fig. 4) can be denoted as ΔP. This value is computed as the difference between P_1 and P_2. P_1 and P_2 refer to the strain values at which the first derivative of $\theta(\varepsilon)$ with respect to ε becomes zero, as determined using eqn (3):

$$P_1, P_2 = -B \pm \frac{\sqrt{B^3 - 3AC}}{3C} \tag{3}$$

By substituting the coefficients of eqn (3) in eqn (4), we obtain:

$$P_1, P_2 = \frac{-E_0}{3(1-\nu)M} \pm \sqrt{\frac{E_0^2}{9(1-\nu)^2M^2} - \frac{2}{3}\frac{A}{r_i(1-\nu)M}} \tag{4}$$

The extent of the plateau zone (eqn (5)) can be calculated using $\Delta P = P_2 - P_1$:

$$\Delta P = \frac{2}{3}\sqrt{\frac{E_0^2}{(1-\nu)^2M^2} + \frac{6A}{r_i(1-\nu)M}} \tag{5}$$

where E_0 can be formulated as $E_0 = 3B_0(1-2\nu)$.[30] We standardized A to 1 because the exact value is unknown and our main goal is to observe the trend of Ga intercalation rather than to determine the specific ΔP value. Table 3 illustrates that the plateau region also diminishes when the number of Ga atoms

increases. More precisely, the transition from 1Ga-mica to 4Ga-mica causes ΔP to drop by around 54% and P2 to drop by about 42%.

Hence, the lower threshold for this non-linear shift, ranging from 1Ga to 4Ga, suggests a faster transition from electron–electron interactions to interactions involving both electrons and phonons. This occurs at a significantly reduced level of strain. Consequently, there is an abrupt and non-linear rise in the stress at this lower strain point, thereby fostering rapid crack propagation under biaxial straining in the presence of Ga. In the end, this phenomenon facilitates mica exfoliation by accelerating the detachment of surface layers from the larger particle.

Experiments involving liquid metal embrittlement of mica by gallium

To validate the results of our first-principles calculations and biaxial straining principles, we conducted an experimental study in which Ga was intercalated into natural bulk mica. The schematic illustration shows bulk mica (Fig. 5(a) and (b)) and Ga immersion between mica layers (Fig. 5(c) and (d)).

The initial insertion of Ga atoms between mica layers was propelled by mechanical forces employed during the ball milling process. According to our DFT calculations, injecting Ga clusters rather than individual atoms is preferable. The insertion of Ga induces biaxial strain in the mica layers, leading to a higher contact angle of the inserted Ga clusters. This, in turn, promotes rapid layer expansion. Simultaneously, the expanded mica layers can be further separated by applying continuous shear force, achieved by keeping the ball milling speed at 600 rpm for 30 min. In addition to the shear force, a compressive force can also be applied to the separated thin mica layers, which also results in thin layers that are smaller in lateral size. After ball milling for 30 minutes, the aggregated mica thin sheets were further separated into individual layers through sonication. Then, the non-exfoliated particles were separated from the sonicated sample by centrifugation at 6000 rpm for 10 minutes, resulting in exfoliated Ga/mica nanosheet composites (Fig. 5(e) and (f)).

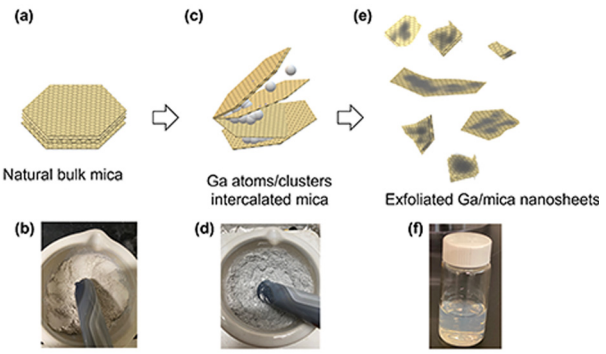

Fig. 5 (a), (b) Natural bulk mica before mixing with Ga and (c), (d) after mixing with Ga. (a), (c) and (e) Schematic illustration of LME on the layered structure of natural bulk mica. (e) and (f) exfoliated 2D nanosheets of mica after LME and sonication.

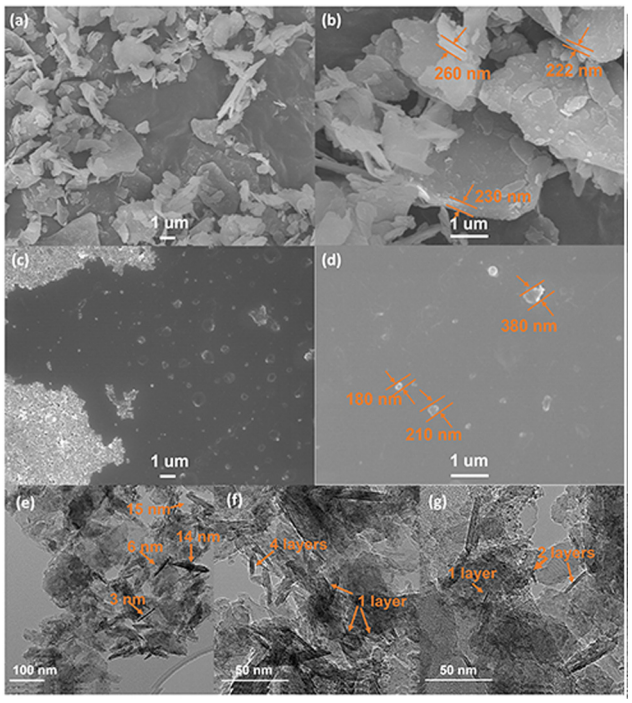

Fig. 6 SEM images of natural bulk mica showcasing (a) low magnification and (b) high magnification, and exfoliated Ga/mica nanosheets showcasing (c) low magnification and (d) high magnification. The TEM images of exfoliated Ga/mica nanosheets showcasing (e) low magnification, (f) and (g) high magnification.

Fig. 6(a) shows the alumina silicate layers of natural mica with an average particle diameter of 2.07 ± 0.70 μm, containing hundreds of layers. The magnified image of the natural mica as shown in Fig. 6(b) provides quantitative thickness information with an average thickness of 293.37 ± 164.20 nm. Exfoliated Ga/mica nanosheet composites show a sheet-like structure with a uniform size in the range of 100–300 nm in width (Fig. 6(c) and (d)). Magnified TEM images of single and few layered nanosheets show a thickness of 1–15 nm (Fig. 6(e)–(g)). The presence of Ga in mica was confirmed by EDS elemental mapping, as shown in Fig. S1 and S2 (ESI†), where the surface atomic percentages of Ga are 0% and 2.1%, Al are 8.1% and 9.4%, Si are 9.5% and 11.3%, O are 79.9% and 74.2%, K are 2.5% and 3.0% for natural bulk mica and the exfoliated Ga/mica nanosheet composite, respectively (S1, ESI†).

Electrical resistance of exfoliated mica

DFT calculations have revealed that the band gap of mica is lowered by the insertion of Ga. This decrease in the electronic band gap facilitates the transition of valence electrons into conduction electrons, acting as charge carriers, thereby enhancing electric current conduction and reducing electrical resistance.

In this study, the measured electrical resistance of cylindrical powder dies made from natural mica and Ga-intercalated mica was found to be 50 ± 8 MΩ and 28 ± 10 MΩ, respectively. This twofold decrease in resistance aligns with the reduction in

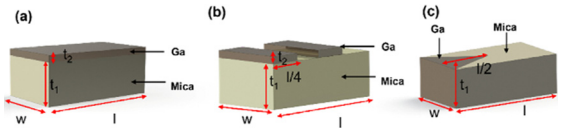

Fig. 7 Schematic of (a) deposition of Ga as a continuous thin film on the mica surface, (b) deposition of Ga as a discontinuous thin film on the mica surface and (c) immersion of Ga in between mica layers.

the band gap from 4.92 eV to 1.25 eV and 0.63 eV for Ga2 and Ga4 clusters, respectively. Despite fixing the amount of added Ga at 10 wt% of the total mica, corresponding to an atomic fraction of 50%, the atomic surface fraction obtained from EDS only indicates a 2% atomic fraction for Ga. This discrepancy could be attributed to Ga incorporation into the interlayers of mica rather than on its surface. Schematic diagrams in Fig. 7 illustrate various ways Ga can be incorporated into mica: (1) continuous deposition as a thin film on the mica surface (Fig. 7(a)), (2) discontinuous deposition as a thin film on the mica surface (Fig. 7(b)), and (3) immersion of Ga between mica layers (Fig. 7(c)).

Based on Ohm's law, resistance of mica for these three types of Ga deposition can be modelled (ESI,† S2) as follows using eqn (6)–(8).

$$R_a = \frac{l\rho_1\rho_2}{(\rho_2 t_1 + \rho_1 t_2)w} \quad (6)$$

$$R_b = \frac{l\rho_1\rho_2}{2w(\rho_2 t_1 + \rho_1 t_2)} + \frac{\rho_1 l}{2wt_1} \quad (7)$$

$$R_c = \frac{l\rho_1\rho_2}{2wt_1(\rho_1 - \rho_2)w}\ln\left(\frac{\rho_1}{\rho_2}\right) + \frac{\rho_1 l}{2wt_1} \quad (8)$$

where l, w, t_1 and ρ_1 are the length, width, thickness, and electrical resistivity of mica, respectively. The electrical resistivity and thickness of Ga layers are ρ_2 and t_2, respectively.

Since $\rho_1 \gg \rho_2$ ($\rho_1 = 1 \times 10^{11}$ to 1×10^{15} and $\rho_2 = 5 \times 10^{-7}$ to 1.4×10^{-7}),[31] the total resistance values given by eqn (7) and (8) are $\sim\rho_1 l/2w_1 t_1$ which are more consistent with the experimental results of halfway reduction of resistance. Nonetheless, it can be inferred from DFT calculations, EDS findings, and resistance measurements that there is a high probability of Ga clusters being in the spaces between the mica layers, which would reduce the band gap and electrical resistance.

CO_2 capturing performance

2D nanomaterials are prodigious candidates for CO_2 adsorption to substitute the traditional adsorbents because of their inherent factors such as ultra-microporous structure, high specific surface area, availability of active sites, and the presence of functional groups for better interaction between the adsorbate and the adsorbent.

Furthermore, T. Van Khai *et al.* reported that the C atom concentration slightly increases during exfoliation, which could be due to the contamination of CO_2 on the exposed mica surface.[9] Therefore, in order to investigate the engineering

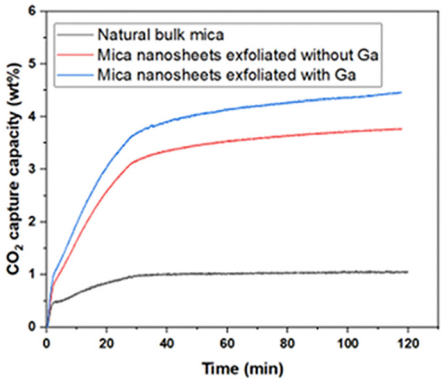

Fig. 8 CO_2 adsorption isotherm at room temperature.

applications of this novel 2D nanomaterial, preliminary CO_2 capture experiments were performed. The CO_2 adsorption capacity of the as-prepared samples was tested at room temperature (30 °C) using TGA. As shown in Fig. 8, the adsorption capacities of natural bulk mica and the Ga/mica nanosheets composite exfoliated using Ga are 1.05% and 4.45%, respectively, representing a significant 4.23-fold increase in adsorption capacity. Moreover, the result was compared with that of the control sample synthesized using the same procedure but without adding Ga. It can be concluded that the addition of Ga enhanced the exfoliation process and led to a 20% increase in CO_2 adsorption capacity compared to the control sample. Additionally, the exfoliated Ga/mica nanosheets demonstrated a significantly higher adsorption of CO_2 (4.45 wt%) compared to N_2 (1.47 wt%), indicating a notable selectivity for CO_2 over N_2 (ESI,† S3). Similar to other clay minerals, exfoliation increases the surface area, active edge, and oncoming ditrigonal cavities which act as CO_2 adsorption sites.[32] The percentage of potassium cations on the surface rises with surface area. The quadrupole interaction between the potassium cations and the CO_2 molecules, as well as the ditrigonal cavities that can trap air molecules, result in the physisorption of CO_2. On the other hand, CO_2 can easily form bonds with the O atoms of the octahedra at the nanosheet edges or be activated to CO_3^{2-} or HCO^{3-} ions by adsorbing H_2O on the mica surface. These carbonates can react by chemisorption with the alkali metal cations on the surface of the 2D nanosheets or in the open space between tetrahedron rings to form K_2CO_3. The formation of K_2CO_3 on the mica surface has been previously reported in experiments,[33] and further insights have been gained through first-principles calculations conducted by our research group.[34] Our study demonstrated that the calculated binding energy between few-layered mica and K_2CO_3 is negative, indicating a favorable interaction. Additionally, we found that K_2CO_3 had a greater affinity for mica nanosheets than for bulk mica.[34] This K_2CO_3 layer enhances electron transfer to CO_2 and facilitates further CO_2 adsorption through physisorption.[7] Moreover, the efficiency of many CO_2 capture systems can be affected by contaminants like water vapor or other organic substances. M. Ali *et al.* reported that the presence of organic acids led to a lower trapping potential due to the reduced wettability of CO_2 on the mica surface. They observed that the wettability decreased further

with an increase in the alkyl chain length in fatty acids, with the wettability of CO_2 ranking as follows: hexanoic acid C_6 > lauric acid C_{12} > stearic acid C_{18} > lignoceric acid C_{24}.[35] On the other hand, CO_2 adsorption on the mica surface was catalysed by water and activated to form CO_3^{2-} or HCO_3^- ions. The potential mechanism of this catalytic surface reaction was initially discussed by K. G. Bhattacharya *et al.* In this process, CO_2 is presumed to attack a hydroxyl site in the outermost tetrahedral layer or H_2O on the surface, leading to the formation of a bicarbonate species. Subsequently, this species would dissociate into a carbonate and a proton, with the proton migrating along the surface.[36] These carbonates can react to form K_2CO_3 on the surface of the 2D nanosheets or in the open space between tetrahedron rings by chemisorption with the alkali metal cations. Thus, these literature data support the notion that both physisorption and chemisorption can cause CO_2 sorption on the surface and between exfoliated mica layers. As a further exploration of increasing CO_2 adsorption capacity, M. Khajeh *et al.* demonstrated an increase in CO_2 adsorption capacity with rising pressure and a decrease with increasing temperature,[37] a phenomenon also observed by M. Lutynski *et al.* for other clays, such as organic carbon (TOC).[38] Our injection of cationic and anionic polymers resulted in a larger adsorption capacity.[39] While there is no existing literature on the effect of amine-functionalization and acid treatment for CO_2 adsorption on mica surfaces, a clay structure similar to mica, montmorillonite (MMT), exhibited a higher CO_2 adsorption capacity following amine-functionalization and acid treatment.[40] Therefore, octadecyl amine modification and acid treatment may hold potential for enhancing the CO_2 adsorption capacity of mica.

Although Ga is used as an intercalation material in the exfoliation of mica to nanosheets, Ga/mica nanosheets could be a promising composite material for CO_2 capture and conversion because aluminosilicate materials/metal composites such as Li–Rh/*y*-zeolite, Cu/SiO_2, Cu–Ni/Al_2O_3 and Cu–Zn/Al_2O_3 have been used in the literature for the conversion of CO_2 to hydrocarbons and other valuable chemicals.[41] However, the performance of these composites can deteriorate if carbonaceous materials adhere to the catalytic metal surface. Theoretically, this issue can be resolved by replacing the metal component with a liquid metal, which is based on the phenomenon of LME, as proved experimentally by J. Tang *et al.*[42] The liquid gallium interface allows the carbonaceous products to be spontaneously exfoliated and removed from the surface of mica through mechanical agitation during the catalyst reaction, maintaining the accessibility of the active sites. During the CO_2 reduction process, Ga (0)s converted into Ga(1), while CO_2 is activated into the $CO_2^{\bullet-}$ radical.[42] Finally, it can be concluded that the Ga/mica nanosheet composite demonstrates good CO_2 adsorption capacity and has promising potential for expanding its CO_2 conversion applications.

Conclusions

In conclusion, we explored combined theoretical, computational, and experimental approaches driven by LME to obtain 2D mica. The new LME-assisted exfoliation of 2D nanosheets utilizes the ability of layer separation by biaxial strain followed by phonon–phonon interaction and reducing the energy barrier for fracture propagation. The DFT calculations have shown that Ga intercalation results in positive tensile strain ε_c, perpendicular to the in-plane direction of mica sheets. This demonstrates a significant shift in the contact angle and suggests that biaxial strain had a noticeable impact. In particular, (1) it leads to a substantial increase in the contact angle of the intercalated liquid metal and (2) the expansion of mica layers caused by the surface tension force of the intercalated liquid metal results in the application of mechanical force. Moreover, DFT calculations have demonstrated that the insertion energy of Ga clusters is lower than that of a single Ga atom and the formation energy of the Ga–mica interface is lower than that of the air–mica interface, indicating a lower energy barrier for the fracture of the mica layer. These findings validate the hypothesis that liquid metal embrittlement (LME) can be used to exfoliate mica through Ga intercalation. Experimental results showed that the exfoliated product consists of single and few layers of mica sheets. Calculations and experiments both showed that the intercalation of Ga into mica decreased the resistance and the band gap. Furthermore, mica nanosheets exfoliated with gallium could be applied for CO_2 capture, and possibly convert it. This is the first time that the liquid embrittlement method has been used to exfoliate a 2D material.

Author contributions

P. Vishakha T. Weerasinghe: methodology, formal analysis, visualization, data curation, writing – original draft preparation, and writing and editing. Shunnian Wu: theoretical simulations, visualization, data curation, writing – original draft preparation, and writing and editing. W. P. Cathie Lee: visualization, writing – review and editing. Qiang Zhu: data curation and resources. Ming Lin: resources, data curation, and writing – review and editing. Ping Wu: conceptualization and biaxial strain modelling, funding acquisition, supervision, project administration, and writing – review and editing.

Conflicts of interest

There are no conflicts to declare.

Acknowledgements

This research was supported through the AME Individual Research Grant (A20E7c0108) by the Agency for Science, Technology and Research, Singapore; MOE2018-T2-1-163 from the Ministry of Education, Singapore; the Marine Science Research and Development program (MSRDP-P28) by the National Research Foundation, Prime Minister's Office, Singapore; the MOE-T1-program (SKI 2022_02_15) from the Ministry of Education, Singapore.

Notes and references

1 Z. Lin, A. McCreary, N. Briggs, S. Subramanian, K. Zhang, Y. Sun, X. Li, N. J. Borys, H. Yuan and S. K. Fullerton-Shirey, *2D Mater.*, 2016, **3**, 042001.
2 A. P. Balan, A. B. Puthirath, S. Roy, G. Costin, E. F. Oliveira, M. Saadi, V. Sreepal, R. Friedrich, P. Serles and A. Biswas, *Mater. Today*, 2022, **58**, 164–200.
3 J. Ding, H. Zhao and H. Yu, *Nanoscale*, 2020, **12**, 16253–16261.
4 H. G. Hansma, *J. Biomol. Struct. Dyn.*, 2013, **31**, 888–895.
5 M. R. Islam and M. Tomitori, *Appl. Surf. Sci.*, 2020, **532**, 147388.
6 X.-F. Pan, H.-L. Gao, Y. Lu, C.-Y. Wu, Y.-D. Wu, X.-Y. Wang, Z.-Q. Pan, L. Dong, Y.-H. Song and H.-P. Cong, *Nat. Commun.*, 2018, **9**, 1–8.
7 P. V. T. Weerasinghe, S. Wu, W. C. Lee, M. Lin, F. Anariba, X. Li, D. H. L. Seng, J. Y. Sim and P. Wu, *Materials*, 2023, **16**, 2921.
8 W. Ying, B. Han, H. Lin, D. Chen and X. Peng, *Nanotechnology*, 2019, **30**, 385705.
9 T. Van Khai, H. G. Na, D. S. Kwak, Y. J. Kwon, H. Ham, K. B. Shim and H. W. Kim, *Nanotechnology*, 2013, **24**, 145602.
10 S. Wu, P. V. T. Weerasinghe and P. Wu, *FlatChem*, 2023, 100565.
11 M. Razmpoosh, C. DiGiovanni, Y. Zhou and E. Biro, *Prog. Mater. Sci.*, 2021, **121**, 100798.
12 T.-J. Tarn and Y. Rasis, *IEEE Trans. Autom. Control*, 1976, **21**, 441–448.
13 C. Ye, Q. Li, P. Wu, G. Tang and W. Liu, 2016.
14 G. Britain and R. J. Parker, *The flixborough disaster: report of the court of inquiry*, HM Stationery Office, 1975.
15 K. Nilsson and A. Hojna, EU Science Hub-European Commission, 2018, 450.
16 M. Rajagopalan, M. Bhatia, M. Tschopp, D. Srolovitz and K. Solanki, *Acta Mater.*, 2014, **73**, 312–325.
17 M. Yamaguchi, T. Tsuru, M. Itakura and E. Abe, *Sci. Rep.*, 2022, **12**, 1–7.
18 G. Kresse and J. Furthmuller, *Phys. Rev. B: Condens. Matter Mater. Phys.*, 1996, **54**, 11169–11186.
19 G. Kresse and J. Furthmuller, *Comput. Mater. Sci.*, 1996, **6**, 15–50.
20 B. Hammer, L. B. Hansen and J. K. Norskov, *Phys. Rev. B: Condens. Matter Mater. Phys.*, 1999, **59**, 7413–7421.
21 G. Kresse and D. Joubert, *Phys. Rev. B: Condens. Matter Mater. Phys.*, 1999, **59**, 1758–1775.
22 S. Grimme, J. Antony, S. Ehrlich and H. Krieg, *J. Chem. Phys.*, 2010, **132**, 19.
23 H. J. Monkhorst and J. D. Pack, *Phys. Rev. B: Solid State*, 1976, **13**, 5188–5192.
24 H. Sakuma, *J. Geophys. Res.: Solid Earth*, 2013, **118**, 6066–6075.
25 A. A. Griffith, *Philos. Trans. R. Soc., A*, 1921, **221**, 163–198.
26 B. T. Tan, P. Wu and F. Anariba, *Results Eng.*, 2022, **13**, 100349.
27 W. C. Lee, S. Wu, F. Anariba and P. Wu, *Mater. Today Adv.*, 2023, **19**, 100406.
28 P. Wu and T. Wu, *J. Alloys Compd.*, 2017, **705**, 269–272.
29 P. Wu, B. T. Tan, J.-I. Jeong, J.-H. Yang, S. Wu and F. Anariba, *J. Alloys Compd.*, 2020, **846**, 156357.
30 R. F. Brady, *Prog. Org. Coat.*, 2001, **43**, 188–192.
31 J. Fowler and F. Farmer, *Nature*, 1955, **175**, 648.
32 K. Sato, K. Fujimoto, W. Dai and M. Hunger, *J. Phys. Chem. C*, 2013, **117**, 14075–14080.
33 J. N. Israelachvili, N. A. Alcantar, N. Maeda, T. E. Mates and M. Ruths, *Langmuir*, 2004, **20**, 3616–3622.
34 S. Wu, W. Lee and P. Wu, *Sci. Rep.*, 2022, **12**, 1–11.
35 M. Ali, A. Aftab, Z.-U.-A. Arain, A. Al-Yaseri, H. Roshan, A. Saeedi, S. Iglauer and M. Sarmadivaleh, *ACS Appl. Mater. Interfaces*, 2020, **12**, 39850–39858.
36 H. K. Christenson and N. H. Thomson, *Surf. Sci. Rep.*, 2016, **71**, 367–390.
37 M. Khajeh and A. Ghaemi, *J. Chin. Chem. Soc.*, 2020, **67**, 253–266.
38 M. Lutyński, P. Waszczuk, P. Słomski and J. Szczepański, *Energy Procedia*, 2017, **125**, 457–466.
39 C. Dai, G. Zhao, Q. You and M. Zhao, *J. Appl. Polym. Sci.*, 2014, **131**(3), DOI: **10.1002/app.39462**.
40 M. Khajeh and A. Ghaemi, *Int. J. Environ. Anal. Chem.*, 2021, 1–26.
41 W. Wang, S. Wang, X. Ma and J. Gong, *Chem. Soc. Rev.*, 2011, **40**, 3703–3727.
42 J. Tang, J. Tang, M. Mayyas, M. B. Ghasemian, J. Sun, M. A. Rahim, J. Yang, J. Han, D. Lawes and R. Jalili, 2020.